Structure of cell–cell adhesion mediated by the Down syndrome cell adhesion molecule

Luqiang Guo[a,b,c,1], Yichun Wu[a,c,1], Haishuang Chang[b], Ze Zhang[a,b,c], Hua Tang[b], Yang Yu[d], Lihui Xin[d], Yingbin Liu[b,e], and Yongning He[a,b,c,e,2]

[a]Shanghai Institute of Biochemistry and Cell Biology, Center for Excellence in Molecular Cell Science, Chinese Academy of Sciences, Shanghai 201210, China; [b]State Key Laboratory of Oncogenes and Related Genes, Shanghai Cancer Institute, Renji Hospital, Shanghai Jiao Tong University School of Medicine, Shanghai 200032, China; [c]University of Chinese Academy of Sciences, Beijing, China; [d]National Facility for Protein Science in Shanghai, Zhangjiang lab, Shanghai Advanced Research Institute, Chinese Academy of Sciences, Shanghai 201210, China; and [e]Department of Biliary-Pancreatic Surgery, Renji Hospital, Shanghai Jiao Tong University School of Medicine, Shanghai 200127, China

Edited by Pamela J. Bjorkman, California Institute of Technology, Pasadena, CA, and approved July 9, 2021 (received for review October 27, 2020)

The Down syndrome cell adhesion molecule (DSCAM) belongs to the immunoglobulin superfamily (IgSF) and plays important roles in neural development. It has a large ectodomain, including 10 Ig-like domains and 6 fibronectin III (FnIII) domains. Previous data have shown that DSCAM can mediate cell adhesion by forming homophilic dimers between cells and contributes to self-avoidance of neurites or neuronal tiling, which is important for neural network formation. However, the organization and assembly of DSCAM at cell adhesion interfaces has not been fully understood. Here we combine electron microscopy and other biophysical methods to characterize the structure of the DSCAM-mediated cell adhesion and generate three-dimensional views of the adhesion interfaces of DSCAM by electron tomography. The results show that mouse DSCAM forms a regular pattern at the adhesion interfaces. The Ig-like domains contribute to both *trans* homophilic interactions and *cis* assembly of the pattern, and the FnIII domains are crucial for the *cis* pattern formation as well as the interaction with the cell membrane. By contrast, no obvious assembly pattern is observed at the adhesion interfaces mediated by mouse DSCAML1 or *Drosophila* DSCAMs, suggesting the different structural roles and mechanisms of DSCAMs in mediating cell adhesion and neural network formation.

DSCAM | cell adhesion | electron tomography | IgSF | cell–cell interaction

The Down syndrome cell adhesion molecule (DSCAM) was initially identified by isolating genes responsible for the phenotypes of Down syndrome (1), a genetic disease featured with cognitive and learning deficits (2). The DSCAM gene locates at the Down syndrome critical region (DSCR) on human chromosome 21 and is broadly expressed in nervous system (1, 3, 4), and its expression increases in patients with Down syndrome and in mouse models (3, 5, 6). Therefore, DSCAM has been hypothesized as a candidate gene associated with neurodevelopmental disorders and its dysregulation may lead to cognitive impairment and intellectual disability in Down syndrome (7), but the mechanism for the association between DSCAM and Down syndrome is still poorly understood.

In invertebrates, *Drosophila* DSCAM1 (dDSCAM1) undergoes extensive alternative splicing by generating 38,016 isoforms with distinct recognition specificity (8–10), which is crucial for isoneuronal avoidance (11, 12). Loss of function or overexpression of dDSCAM1 in mutant flies causes defects or disorders in dendrite arborization (13, 14), axon guidance (15, 16), axon branching (17, 18), and synaptic targeting (11, 19, 20). *Drosophila* DSCAM2 (dDSCAM2) and DSCAM4 (dDSCAM4) also function in neural network formation by directing dendritic targeting but without the massive isoform diversity (21), and dDSCAM2 can mediate axonal tiling as well (22). *Aplysia* DSCAM (aDSCAM) is involved in transsynaptic protein localization (23).

In vertebrates, two paralogous DSCAM genes, DSCAM and DSCAML1 (DSCAM-LIKE1) were identified (1, 24) and both of them could promote isoneuronal and homotypic self-avoidance (25, 26). In mouse, neurons expressing DSCAM (mDSCAM) or DSCAML1 (mDSCAML1) mutants may lose their mosaic pattern and neurite arborization (26, 27). Although the mechanism of mDSCAM-mediated self-avoidance remains unclear, it has been suggested that mDSCAM may function by masking the adhesion mediated by certain cadherin superfamily members (28). In addition, mDSCAM may also regulate neurite outgrowth (29, 30), promote cell death (31, 32), and control neuronal delamination (33). Studies have also shown that it could direct lamina-specific synaptic connections in chick (34) and be involved in cell movement in zebrafish (35). In contrast to dDSCAM1, the extensive alternative splicing has not been found for DSCAM in vertebrates, suggesting the different roles in the formation of neuronal circuits.

DSCAM belongs to the immunoglobulin superfamily (IgSF) and consists of 10 immunoglobulin-like (Ig-like) domains, 6 type III fibronectin (FnIII) domains, a transmembrane domain, and a cytoplasmic domain (Fig. 1*A*). The domain arrangements of DSCAMs from invertebrates and vertebrates are quite similar, and the amino acid sequence identities of DSCAM among homologs are 98% between mDSCAM and hDSCAM (human), 59% between mDSCAM and mDSCAML1, and 33% between mDSCAM and dDSCAM1. The crystal structures of the N-terminal Ig-like domains of dDSCAM1 have been solved (36, 37). The eight N-terminal Ig-like

Significance

The Down syndrome cell adhesion molecule (DSCAM) is broadly expressed in the nervous system and functions in neural development and network formation by mediating homophilic adhesion between cells. Here we explored the in situ assembly of DSCAM using multiple biochemical and biophysical methods and found that mouse DSCAM is well organized at the adhesion interfaces by forming a regular pattern. Both Ig-like domains and fibronectin III domains contribute to the regular pattern formation but have different roles. By contrast, mouse DSCAML1 or *Drosophila* DSCAMs do not show similar patterns at the adhesion interfaces. These results suggest that DSCAMs might have different structural roles and mechanisms in regulating neural network formation, which may be associated with corresponding disorders in neural development.

Author contributions: L.G. and Y.H. designed research; L.G., Y.W., H.C., Z.Z., H.T., Y.Y., and L.X. performed research; Y.Y., L.X., and Y.L. contributed new reagents/analytic tools; L.G., Y.W., Y.L., and Y.H. analyzed data; and L.G., Y.W., and Y.H. wrote the paper.

The authors declare no competing interest.

This article is a PNAS Direct Submission.

[1]L.G. and Y.W. contributed equally to this work.

[2]To whom correspondence may be addressed. Email: he@sibcb.ac.cn.

This article contains supporting information online at https://www.pnas.org/lookup/suppl/doi:10.1073/pnas.2022442118/-/DCSupplemental.

Published September 16, 2021.

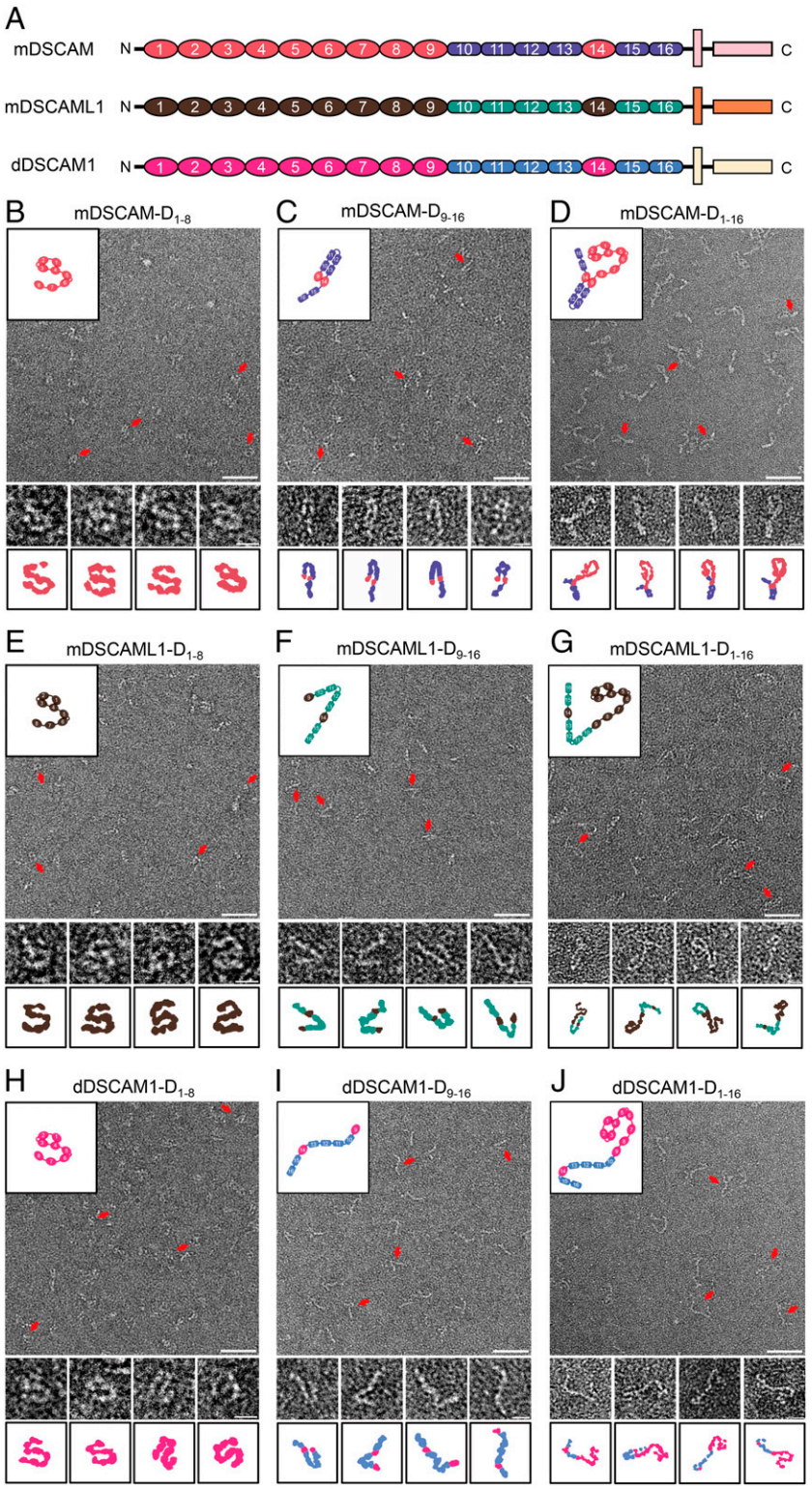

Fig. 1. Conformations of the ectodomains of mDSCAM, mDSCAML1, and dDSCAM1. (*A*) Diagrams of mDSCAM, mDSCAML1, and dDSCAM1 (ovals, Ig-like domains; rounded rectangles, FnIII domains; vertical rectangles, transmembrane domains; rectangles, cytoplasmic domains). (*B–D*) Negative staining EM images show the particles of mDSCAM-$D_{1–8}$, mDSCAM-$D_{9–16}$, and mDSCAM-$D_{1–16}$, respectively (*Top*, red arrows). (Scale bar, 50 nm.) The selected particles (*Middle*; the particles are picked from different images) and their contours (*Bottom*) are also listed. (Scale bar, 10 nm.) The schematic models of mDSCAM-$D_{1–8}$, mDSCAM-$D_{9–16}$, and mDSCAM-$D_{1–16}$ are shown in the *Top Left Insets*, respectively. (*E–G*) Negative staining EM images show the particles of mDSCAML1-$D_{1–8}$, mDSCAML1-$D_{9–16}$, and mDSCAML1-$D_{1–16}$, respectively (*Top*, red arrows). (Scale bar, 50 nm.) The selected particles (*Middle*) and their contours (*Bottom*) are also listed. (Scale bar, 10 nm.) The schematic models of mDSCAML1-$D_{1–8}$, mDSCAML1-$D_{9–16}$, and mDSCAML1-$D_{1–16}$ are shown in the *Top Left Insets*, respectively. (*H–J*) Negative staining EM images show the particles of dDSCAM1-$D_{1–8}$, dDSCAM1-$D_{9–16}$, and dDSCAM1-$D_{1–16}$, respectively (*Top*, red arrows). (Scale bar, 50 nm.) The selected particles (*Middle*) and their contours (*Bottom*) are also listed. (Scale bar, 10 nm.) The schematic models of dDSCAM1-$D_{1–8}$, dDSCAM1-$D_{9–16}$, and dDSCAM1-$D_{1–16}$ are shown in the *Top Left Insets*, respectively.

domains form a dimer with a double-S–shaped conformation, which is critical for the homophilic cell adhesion (36). However, it is unclear whether the N-terminal Ig-like domains of mDSCAM and mDSCAML1 adopt a similar conformation to dDSCAM1, and the roles of other domains of DSCAM in cell adhesion remain elusive.

Recently, electron tomography (ET) has become a powerful tool to provide three-dimensional (3D) views of biological samples (38, 39). By combining correlative light and electron microscopy (CLEM), high-pressure freezing and freeze substitution (HPF-FS), ultrathin sectioning and ET, the 3D structure of cellular or tissue samples can be reconstructed at nanometer resolution, revealing the molecular architecture of macromolecules in situ (40–43). Here we characterize the structures of mDSCAM, mDSCAML1, and dDSCAMs by electron microscopy (EM) as well as other biochemical and biophysical methods and reconstruct the 3D views

of the mDSCAM-mediated adhesion interface by electron tomography, thereby unveiling the in situ structural model and the potential mechanism of cell adhesion by DSCAM.

Results

The Conformations of the Ectodomains of mDSCAM, mDSCAML1, and dDSCAM1. In order to compare the conformations of DSCAMs from mouse and *Drosophila*, fragments containing the eight N-terminal Ig-like domains ($D_{1–8}$), including mDSCAM-$D_{1–8}$, mDSCAML1-$D_{1–8}$, and dDSCAM1-$D_{1–8}$, were expressed in HEK293 cells and insect cells, respectively (*SI Appendix*, Fig. S1*A*). The purified proteins were negatively stained and imaged by electron microscopy (Fig. 1 *B*, *E*, and *H* and *SI Appendix*, Fig. S1*B*). EM images showed that although the particles revealed certain flexibility, an S-shaped conformation could be seen for most of the particles of mDSCAM-$D_{1–8}$ (Fig. 1*B* and *SI Appendix*, Fig. S1*B*), mDSCAML1-$D_{1–8}$ (Fig. 1*E* and *SI Appendix*, Fig. S1*B*), and dDSCAM1-$D_{1–8}$ (Fig. 1*H* and *SI Appendix*, Fig. S1*B*). This was consistent with the known crystal structure of the N-terminal fragments of dDSCAM1 (36), suggesting that mDSCAM and mDSCAML1 might also form double-S–shaped homophilic dimers during cell adhesion.

In parallel, we also expressed and purified the fragments of $D_{9–16}$ of DSCAMs, including mDSCAM-$D_{9–16}$, mDSCAML1-$D_{9–16}$, and dDSCAM1-$D_{9–16}$ (*SI Appendix*, Fig. S1*C*), and imaged the fragments under EM after negative staining (Fig. 1 *C*, *F*, and *I* and *SI Appendix*, Fig. S1*D*). Interestingly, the EM images of mDSCAM-$D_{9–16}$ revealed a hairpin-like conformation with a long arm and a short arm (Fig. 1*C* and *SI Appendix*, Fig. S1*D*). The short arm was about 12 nm, roughly equal to the length of three Ig-like or FnIII domains, and the long arm was about 20 nm, roughly equal to the length of five Ig-like or FnIII domains. By contrast, the conformations of the fragments of mDSCAML1-$D_{9–16}$ and dDSCAM1-$D_{9–16}$ were rather flexible (Fig. 1 *F* and *I* and *SI Appendix*, Fig. S1*D*). It was noticeable that a kink could be seen in the fragment of mDSCAML1-$D_{9–16}$, suggesting that it might resemble mDSCAM-$D_{9–16}$ in some degree, but no stable hairpin-like conformation was observed for mDSCAML1-$D_{9–16}$ (Fig. 1*F* and *SI Appendix*, Fig. S1*D*). In addition, the size exclusion chromatography (SEC) profiles of the three fragments also showed that mDSCAM-$D_{9–16}$ might have a more compact conformation than mDSCAML1-$D_{9–16}$ and dDSCAM1-$D_{9–16}$, as it had a larger elution volume than the other two fragments despite having similar molecular weights (*SI Appendix*, Fig. S1*C*), consistent with the EM images shown above.

In order to visualize the conformations of the intact ectodomains of DSCAMs, mDSCAM-$D_{1–16}$, mDSCAML1-$D_{1–16}$, and dDSCAM1-$D_{1–16}$ were also expressed and purified (*SI Appendix*, Fig. S1*E*) and imaged under EM after negative staining. The resulting images showed that mDSCAM-$D_{1–16}$ could be roughly divided into a head and a tail (Fig. 1*D* and *SI Appendix*, Fig. S1*F*). The head was similar to the particles of mDSCAM-$D_{1–8}$ (Fig. 1*B* and *SI Appendix*, Fig. S1*B*), which had an S-shaped conformation, while the tail adopted a hairpin-like conformation (Fig. 1*D* and *SI Appendix*, Fig. S1*F*), as revealed by the images of mDSCAM-$D_{9–16}$ (Fig. 1*C* and *SI Appendix*, Fig. S1*D*). By comparing the conformation of mDSCAM-$D_{9–16}$ (Fig. 1*C* and *SI Appendix*, Fig. S1*D*) with the tail portion of mDSCAM-$D_{1–16}$ (Fig. 1*D* and *SI Appendix*, Fig. S1*F*), it would be reasonable to assign $D_{12–16}$ as the long arm and $D_{9–11}$ as the short arm of the hairpin (Fig. 1*C*). The EM images of mDSCAML1-$D_{1–16}$ (Fig. 1*G* and *SI Appendix*, Fig. S1*F*) and dDSCAM1-$D_{1–16}$ (Fig. 1*J* and *SI Appendix*, Fig. S1*F*) showed that they also had similar S-shaped heads to mDSCAM-$D_{1–16}$ (Fig. 1*D* and *SI Appendix*, Fig. S1*F*), consistent with the images of mDSCAML1-$D_{1–8}$ (Fig. 1*E* and *SI Appendix*, Fig. S1*B*) and dDSCAM1-$D_{1–8}$ (Fig. 1*H* and *SI Appendix*, Fig. S1*B*), respectively. However, the tail parts of mDSCAML1-$D_{1–16}$ (Fig. 1*G* and *SI Appendix*, Fig. S1*F*) and dDSCAM1-$D_{1–16}$ (Fig. 1*J* and *SI Appendix*, Fig. S1*F*) appeared to have heterogeneous conformations and to be more flexible than the tail of mDSCAM-$D_{1–16}$ (Fig. 1*D* and *SI Appendix*, Fig. S1*F*), which was consistent with the images of mDSCAML1-$D_{9–16}$ (Fig. 1*F* and *SI Appendix*, Fig. S1*D*) and dDSCAM1-$D_{9–16}$ (Fig. 1*I* and *SI Appendix*, Fig. S1*D*), respectively.

Another feature regarding the ectodomains of DSCAMs was that all the in vitro expressed fragments appeared to be monomeric, as indicated by the EM images (Fig. 1 and *SI Appendix*, Fig. S1 *B*, *D*, and *F*) as well as the SEC profiles (*SI Appendix*, Fig. S1 *A*, *C*, and *E*), suggesting that the dimeric interactions of DSCAM molecules might be relatively weak and the homodimers only formed at the adhesion interfaces between the cell membranes. This was consistent with previous evidence showing that the clustering of dDSCAM1 was required for binding assays due to the weak interaction between monomers (10).

mDSCAM Forms a Regular Pattern at the Cell Adhesion Interface. To visualize the structure of cell adhesion interface mediated by mDSCAM, HEK293T cells were transfected with the full length of mDSCAM (mDSCAM-$D_{1–16}$ [FL]) and imaged by fluorescent microscopy (Fig. 2 *A* and *B*). The images showed that the transfected cells could form adhesion interfaces highlighted by fluorescence between adjacent cells (Fig. 2*B*). To explore the structural details of the adhesion interfaces, the transfected cells were cultured on dishes with carbon markers (Fig. 2*C*) and subject to chemical fixation and semithin sectioning. The cells identified for forming adhesion pairs could be located on the semithin sections according to the carbon markers and cell growing patterns (Fig. 2*D*), then ultrathin sections were prepared for electron microscopic imaging (43, 44) (Fig. 2*E*). The resulting EM images showed a regular density pattern at the interfaces between the neighboring cells (Fig. 2*E*), suggesting that mDSCAM could be assembled regularly in *cis* along the adhesion interfaces.

To explore the details of the regular pattern identified above, HPF-FS was utilized to improve the sample preservation quality (42, 43). Indeed, the ultrathin sections prepared by HPF-FS showed more details of the regular pattern and the two leaflets of the cell membranes could also be visualized clearly (Fig. 2*F* and *SI Appendix*, Fig. S2). The pattern had a series of parallel rod-like densities with an approximate 60-degree tilt angle to the cell membrane (Fig. 2*F* and *SI Appendix*, Fig. S2*A*), which was different from the patterns observed between the nontransfected HEK293 cells (*SI Appendix*, Fig. S3) or formed by other adhesion molecules published before (43, 45, 46), and the intermembrane distance was about 23 nm (see Fig. 4*E*). Besides the tilted rod-liked pattern, other patterns were also observed at different adhesion interfaces by mDSCAM (Fig. 2*G* and *SI Appendix*, Fig. S2). Since the sectioning was performed randomly for a 3D interface, the resulting two-dimensional (2D) patterns might correspond to projections at different angles. Indeed, after inspecting a number of interfaces using electron tomography (*SI Appendix*, Fig. S10), these patterns were identified with different tilt angles in different tilt series or tomograms (*SI Appendix*, Fig. S10 and Movie S1), suggesting that mDSCAM molecules were assembled similarly at different interfaces.

No Regular Pattern Is Identified for mDSCAML1 and dDSCAMs at the Adhesion Interfaces. To examine the structure of mDSCAML1-mediated cell interface, mDSCAML1 (mDSCAML1-$D_{1–16}$ [FL])-transfected cells were imaged by fluorescent microscopy and EM using similar procedures described above (Fig. 3 *A–F* and *SI Appendix*, Fig. S4 *A–E*). The fluorescent images showed that adhesion interfaces could form between the mDSCAML1-transfected cells; however, unlike mDSCAM, no regular pattern was identified for mDSCAML1 between the cell membranes (Fig. 3 *C–F* and *SI Appendix*, Fig. S4 *D* and *E*). The intermembrane distance of the mDSCAML1-mediated cell interfaces was about 20 nm (Fig. 3*M*), slightly shorter than the width of 23 nm for mDSCAM (Fig. 4*E*).

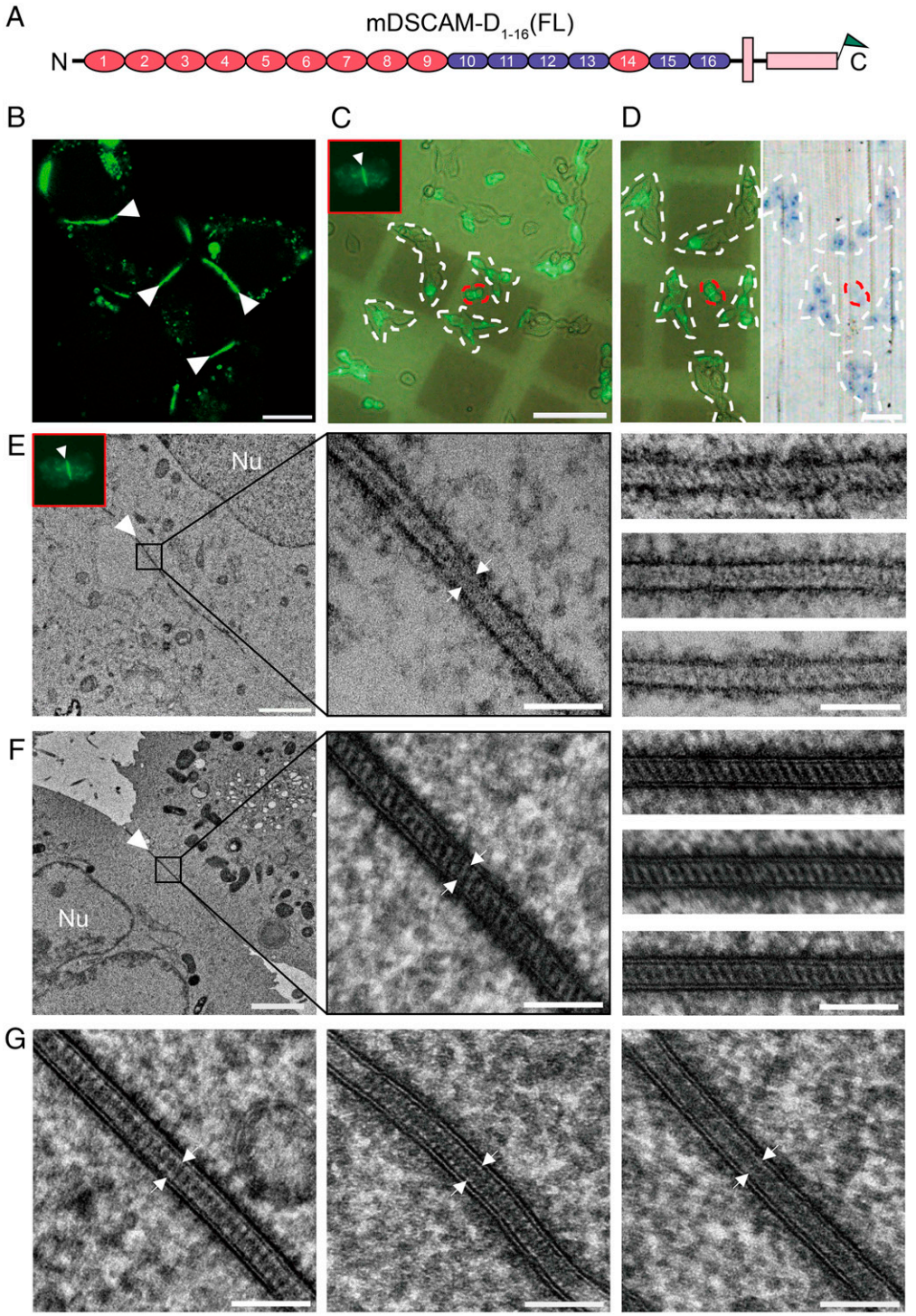

Fig. 2. Light and electron microscopy of the mDSCAM-mediated cell adhesion interfaces. (*A*) Diagram of mDSCAM fused with GFP (green triangle) at the C terminus. (*B*) A confocal fluorescent image shows the formation of the mDSCAM-mediated adhesion interfaces between the transfected HEK293 cells (white arrowheads). (Scale bar, 10 μm.) (*C*) The mDSCAM-transfected HEK293 cells form clusters (white dashed lines) on a marked cell culture dish (dark square) under a fluorescent-light microscope. (Scale bar, 100 μm.) A pair of cells with an adhesion interface in between is marked by red dashed lines and also shown in the *Top Left Inset* (white arrowhead). (*D*) Correlation of the marked cells visualized by fluorescent-light microscopy (*Left*, white and red dashed lines; also shown in *C*) with the cells identified on a plastic embedded semithin section for EM imaging (*Right*, white and red dashed lines). (Scale bar, 50 μm.) (*E*) An EM image of the adhesion interface identified by fluorescent microscopy (*Inset*, also shown in *C* and *D*). The interface is indicated by a white arrowhead (*Left*). Nu, nucleus. (Scale bar, 2 μm.) The enlarged interface is also shown (*Middle*, black square) and the intermembrane spacing is indicated by a pair of white arrows. (Scale bar, 100 nm.) A gallery of EM images of the mDSCAM-mediated adhesion interfaces prepared by CLEM and chemical fixation is shown on the *Right*. (Scale bar, 100 nm.) (*F*) An EM image of the mDSCAM-mediated adhesion interface prepared by HPF-FS. The interface is indicated by a white arrowhead (*Left*). Nu, nucleus. (Scale bar, 2 μm.) The enlarged interface is also shown (*Middle*, black square) and the intermembrane spacing is indicated by a pair of white arrows. (Scale bar, 100 nm.) A gallery of EM images of the mDSCAM-mediated adhesion interfaces prepared by HPF-FS is shown on the *Right*. (Scale bar, 100 nm.) (*G*) EM images show the alternative projections of the mDSCAM-mediated adhesion interfaces. (Scale bar, 100 nm.)

Due to the broad expression of mDSCAM and mDSCAML1 in the nervous system (1, 24), we cotransfected cells with mDSCAM and mDSCAML1 fused with GFP and mCherry tag, respectively, and examined the adhesion interfaces (*SI Appendix*, Fig. S4 *F–M*). Indeed, the interfaces containing both molecules were identified by fluorescent microscopy (*SI Appendix*, Fig. S4*F*), but no obvious regular pattern was observed in the EM images (*SI Appendix*, Fig. S4 *J–M*) and the intermembrane distance was 27 nm, larger than that for mDSCAM or mDSCAML1, suggesting that mDSCAML1 might interfere with the ordered assembly of mDSCAM, thus having regulatory activities for each other.

The dDSCAM1 mediated cell adhesion was also explored by transfecting *Drosophila* S2 cells with the full-length dDSCAM1 fused with GFP (dDSCAM1-$D_{1–16}$ [FL]) (Fig. 3*G*). The highlighted adhesion interfaces could be visualized by fluorescent microscopy (Fig. 3*H* and *SI Appendix*, Fig. S5*B*); then the similar procedures were applied to the S2 cells for EM imaging (Fig. 3 *I–L* and *SI Appendix*, Fig. S5). The resulting images showed that dDSCAM1 had a similar intermembrane distance (about 24 nm) to mDSCAM (Figs. 3*M* and 4*E*), but no obvious pattern was observed at the adhesion interfaces (Fig. 3 *I–L* and *SI Appendix*, Fig. S5 *E* and *F*), similar to the case of mDSCAML1 (Fig. 3 *C–F* and *SI Appendix*, Fig. S4 *D* and *E*). To verify the results, we also examined the adhesion interfaces mediated by a series of truncation mutants of dDSCAM1 (*SI Appendix*, Fig. S5). The data showed that no regular pattern was observed for all of the mutants (*SI Appendix*, Fig. S5 *E* and *F*), and the intermembrane distances increased as the number of domains included in the mutants (*SI Appendix*, Fig. S5*G*), this could be explained by the observation from the EM images showing that dDSCAM1 was quite flexible except the N-terminal Ig-like domains, therefore more domains included in the fragments would lead to larger intermembrane distances.

To further test the formation of the assembly pattern, we generated two chimeric molecules by swapping the ectodomains of mDSCAM (mDM_{ecto}) with dDSCAM1 (dDM_{ecto}). The resulting molecules, dDM_{ecto}-mDM_{cyto} and mDM_{ecto}-dDM_{cyto} (*SI Appendix*, Fig. S9*A*),

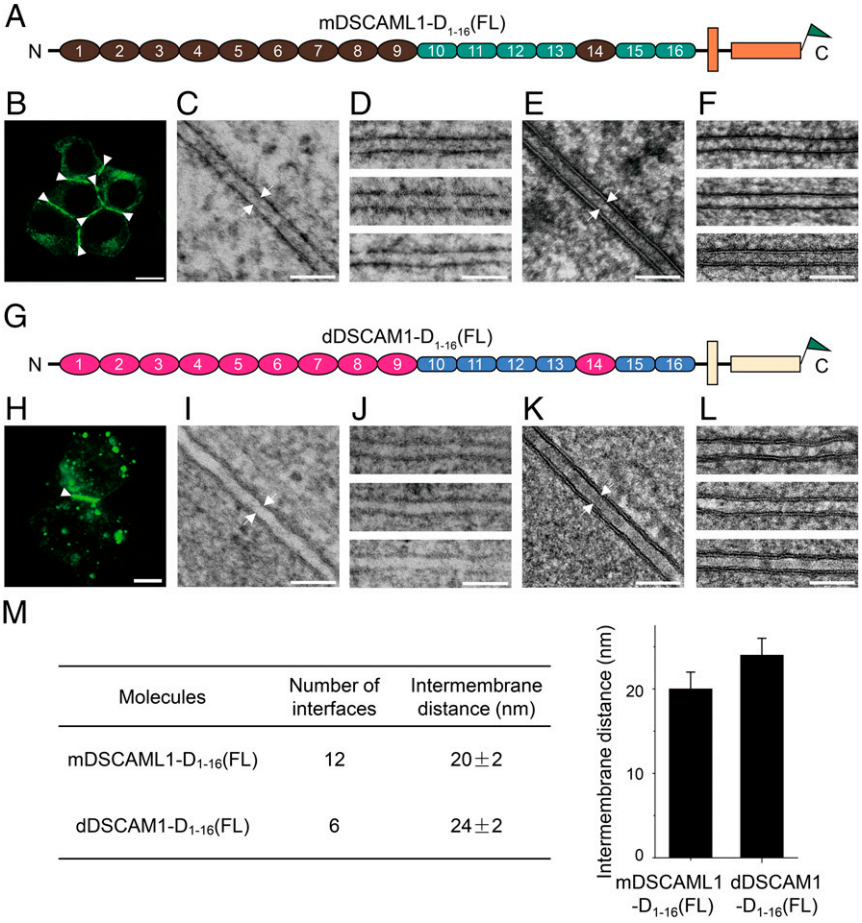

Molecules	Number of interfaces	Intermembrane distance (nm)
mDSCAML1-D_{1-16}(FL)	12	20±2
dDSCAM1-D_{1-16}(FL)	6	24±2

Fig. 3. Light and electron microscopy of the mDSCAML1- and dDSCAM1-mediated cell adhesion interfaces. (*A*) Diagram of mDSCAML1 fused with GFP (green triangle) at the C terminus. (*B*) A confocal fluorescent image shows the formation of the mDSCAML1-mediated adhesion interfaces between the transfected HEK293 cells (white arrowheads). (Scale bar, 10 μm.) (*C*) An EM image of the adhesion interface of mDSCAML1 identified by CLEM and chemical fixation. The intermembrane spacing is indicated by a pair of white arrows. (Scale bar, 100 nm.) (*D*) A gallery of EM images of the mDSCAML1-mediated adhesion interfaces prepared by CLEM and chemical fixation. (Scale bar, 100 nm.) (*E*) An EM image of the adhesion interface of mDSCAML1 prepared by HPF-FS. The intermembrane spacing is indicated by a pair of white arrows. (Scale bar, 100 nm.) (*F*) A gallery of EM images of the mDSCAML1-mediated adhesion interfaces prepared by HPF-FS. (Scale bar, 100 nm.) (*G*) Diagram of dDSCAM1 fused with GFP (green triangle) at the C terminus. (*H*) A confocal fluorescent image shows the formation of the dDSCAM1-mediated adhesion interfaces between the transfected *Drosophila* S2 cells (white arrowheads). (Scale bar, 10 μm.) (*I*) An EM image of the adhesion interface of dDSCAM1 identified by CLEM and chemical fixation. The intermembrane spacing is indicated by a pair of white arrows. (Scale bar, 100 nm.) (*J*) A gallery of EM images of the dDSCAM1-mediated adhesion interfaces prepared by CLEM and chemical fixation. (Scale bar, 100 nm.) (*K*) An EM image of the adhesion interface of dDSCAM1 prepared by HPF-FS. The intermembrane spacing is indicated by a pair of white arrows. (Scale bar, 100 nm.) (*L*) A gallery of EM images of the dDSCAM1-mediated adhesion interfaces prepared by HPF-FS. (Scale bar, 100 nm.) (*M*) Statistics of the intermembrane distances of the adhesion interfaces mediated by mDSCAML1 and dDSCAM1.

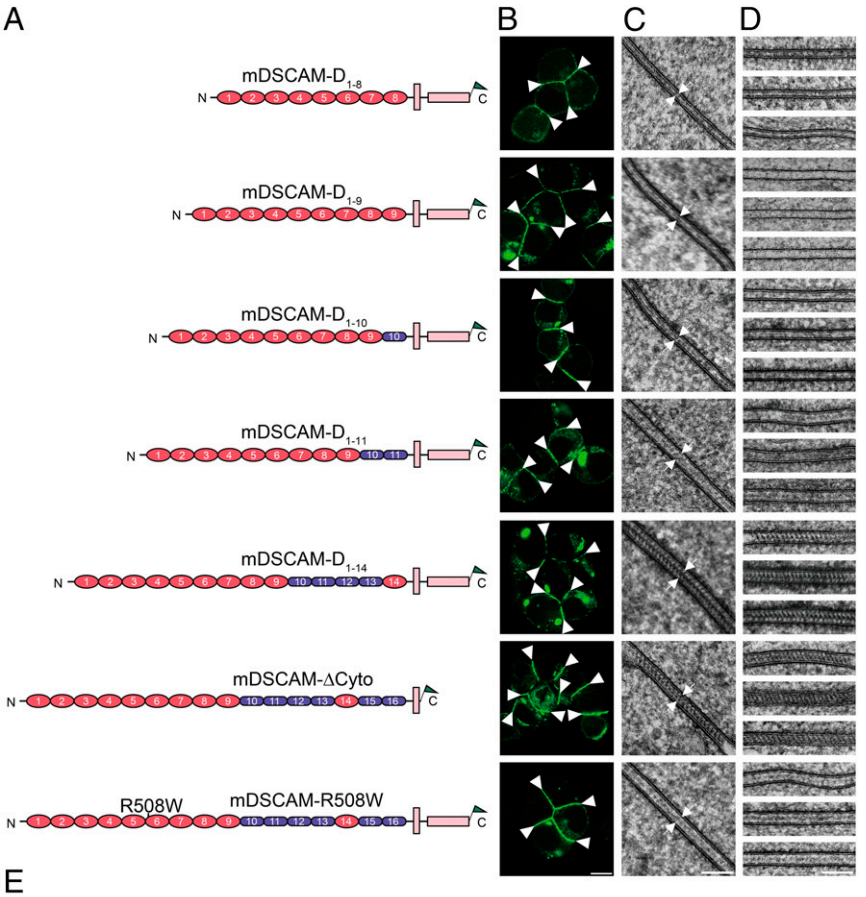

E

Molecules	Number of interfaces	Intermembrane distance (nm)
mDSCAM-D_{1-8}	6	11±1
mDSCAM-D_{1-9}	12	16±1
mDSCAM-D_{1-10}	10	19±1
mDSCAM-D_{1-11}	7	25±2
mDSCAM-D_{1-14}	12	28±2
mDSCAM-D_{1-16}(FL)	10	23±1
mDSCAM-ΔCyto	14	23±2
mDSCAM-R508W	10	26±2

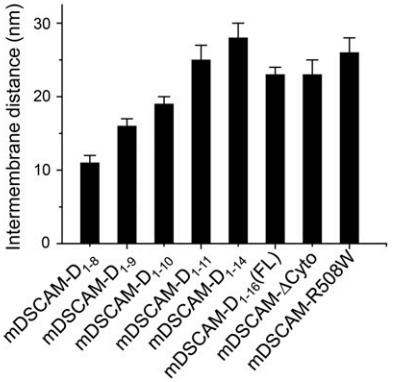

Fig. 4. Light and electron microscopy of the cell adhesion interfaces mediated by the mDSCAM mutants. (*A*) Diagrams of the mDSCAM mutants fused with GFP (green triangle) at the C termini. (*B*) Fluorescent confocal images show the formation of adhesion interfaces between the HEK293 cells transfected with the mDSCAM mutants (white arrowheads). (Scale bar, 10 μm.) (*C*) EM images of the adhesion interfaces of the mDSCAM mutants prepared by HPF-FS. The intermembrane spacing is shown by a pair of white arrows in each image. (Scale bar, 100 nm.) (*D*) A gallery of EM images of the adhesion interfaces of the mDSCAM mutants prepared by HPF-FS. (Scale bar, 100 nm.) (*E*) Statistics of the intermembrane distances of the adhesion interfaces mediated by the mDSCAM mutants.

were transfected with HEK293 cells and S2 cells, respectively. Although cell adhesion could be formed by the two chimeric molecules, no regular pattern was identified in the interfaces in either case (*SI Appendix*, Fig. S9 *B* and *C*) and the intermembrane distances were also changed, suggesting that the difference between mammalian and insect expression systems, for example, carbohydrate modification, might also affect the assembly pattern formation of DSCAM at the adhesion interfaces.

In addition, we examined the adhesion interfaces formed by dDSCAM2, dDSCAM4, and aDSCAM following similar procedures. The results showed that none of these molecules form regular assembly pattern at the adhesion interfaces (*SI Appendix*, Fig. S6), suggesting that mDSCAM might be unique among DSCAM homologs in mediating adhesion between cells.

The 14 N-terminal Domains of mDSCAM Are Required for the Regular Pattern Formation at the Adhesion Interfaces. To characterize the regular pattern assembly of mDSCAM, we generated a series of truncation mutants of mDSCAM and visualized the adhesion interfaces by both fluorescent microscopy and EM (Fig. 4). First of all, the cytoplasmic domain of mDSCAM was removed (mDSCAM-ΔCyto), and the fluorescent images showed that the cell adhesion interfaces could still be formed by this mutant (Fig. 4 *A* and *B* and *SI Appendix*, Fig. S7*A*). Moreover, EM results

showed that mDSCAM-ΔCyto could also form a similar regular pattern with almost identical intermembrane distances as the wild type (Fig. 4 *C*–*E* and *SI Appendix*, Fig. S7 *D* and *E*), suggesting that the cytoplasmic domain was not required for the assembly of mDSCAM on the cell membranes.

Then we made a number of mutants of the ectodomain of mDSCAM to test the adhesion formation (Fig. 4*A*). The fluorescent images showed that all the truncation mutants could induce cell–cell adhesion (Fig. 4*B* and *SI Appendix*, Fig. S7*A*). Among them, mDSCAM-$D_{1–8}$ had the shortest ectodomain, suggesting that the eight N-terminal Ig-like domains were sufficient for inducing cell adhesion (Fig. 4*B* and *SI Appendix*, Fig. S7*A*). This was similar to the reported data for dDSCAM1-$D_{1–8}$, where dDSCAM1-$D_{1–8}$ could introduce homophilic adhesion through the double-S–shaped dimers (9, 36). In addition, the intermembrane distance of the mDSCAM-$D_{1–8}$–mediated interface was about 11 nm (Fig. 4*E*), similar to the width of the dDSCAM1-$D_{1–8}$–mediated cell interfaces (*SI Appendix*, Fig. S5*G*) as well as the length of dDSCAM1-$D_{1–8}$ in the crystal structure (36), suggesting that mDSCAM-$D_{1–8}$ might also form similar double-S–shaped homodimers at the adhesion interfaces.

However, the EM images showed that no regular pattern was formed at the adhesion interfaces unless the 14 N-terminal domains were included in the mutants (Fig. 4 *C* and *D* and *SI Appendix*, Fig. S7 *D* and *E*). The pattern identified in the mDSCAM-$D_{1–14}$–mediated cell interfaces (Fig. 4 *C* and *D* and *SI Appendix*, Fig. S7 *D* and *E*) was similar to that of the full-length mDSCAM (Fig. 2*F* and *SI Appendix*, Fig. S2), suggesting that the 14 N-terminal

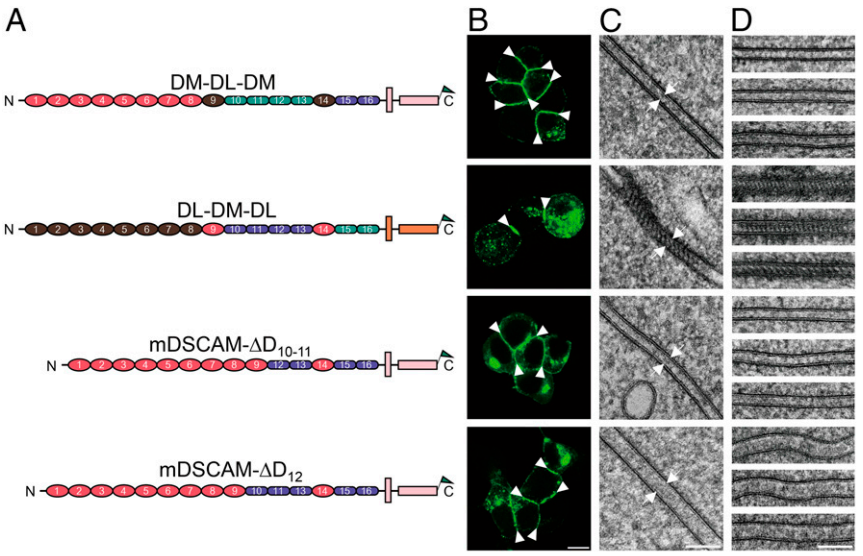

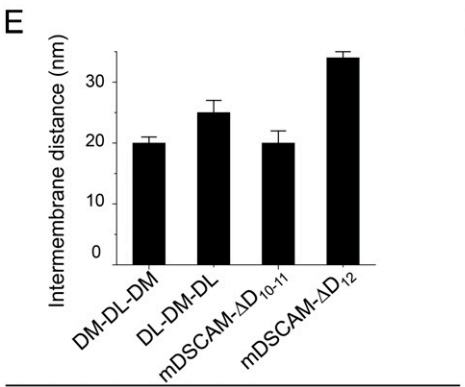

Molecules	Number of interfaces	Intermembrane distance (nm)
DM-DL-DM	13	20±1
DL-DM-DL	12	25±2
mDSCAM-ΔD$_{10-11}$	9	20±2
mDSCAM-ΔD$_{12}$	10	34±1

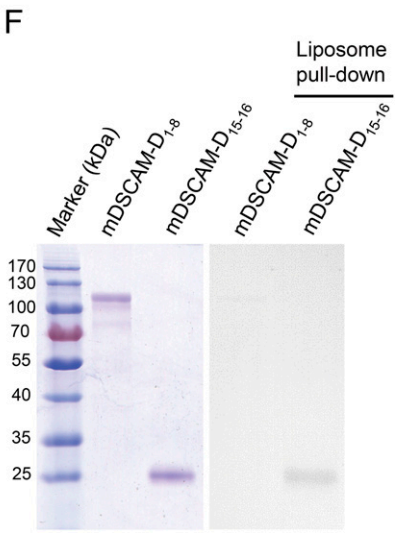

Fig. 5. Light and electron microscopy of the cell adhesion interfaces mediated by the mDSCAM/mDSCAML1 chimeric molecules and the FnIII domain deletion mutants of mDSCAM. (*A*) Diagrams of the mDSCAM/mDSCAML1 chimeric molecules and the FnIII domain deletion mutants of mDSCAM fused with GFP (green triangle) at the C termini. (*B*) Fluorescent confocal images show the formation of adhesion interfaces between the HEK293 cells transfected with the mDSCAM mutants (white arrowheads). (Scale bar, 10 μm.) (*C*) EM images of the adhesion interfaces of the mDSCAM mutants prepared by HPF-FS. The intermembrane spacing is shown by a pair of white arrows in each image. (Scale bar, 100 nm.) (*D*) A gallery of EM images of the adhesion interfaces of the mDSCAM mutants prepared by HPF-FS. (Scale bar, 100 nm.) (*E*) Statistics of the intermembrane distances of the adhesion interfaces mediated by the DSCAM mutants. (*F*) The SDS-PAGE of the fragments of mDSCAM-$D_{1–8}$ and mDSCAM-$D_{15–16}$ (*Left*) and the Western blot result showing that the fragment of mDSCAM-$D_{15–16}$ can be pulled down by the liposomes (*Right*).

domains were necessary for the regular *cis* pattern formation at the interface. Furthermore, the intermembrane distances of the adhesion interfaces mediated by the mutants were also measured and it showed that the distances increased with the number of domains included in the mutants and reached about 28 nm for the mDSCAM-$D_{1–14}$–mediated interface (Fig. 4*E*). Interestingly, the intermembrane distance maintained by the intact ectodomain (mDSCAM-$D_{1–16}$ or mDSCAM-ΔCyto) decreased to about 23 nm (Fig. 4*E*), suggesting that domains $D_{15–16}$ might have a role in reducing the intermembrane spacing.

It has been shown that residue R496 on the Ig6 of dDSCAM1 played an important role in maintaining the N-terminal S-shaped conformation, and the single mutation R496W could reduce homophilic binding, and generated a loss-of-function phenotype of dDSCAM1 (36). Since this residue was conserved for mDSCAM (R508), we constructed a single mutant R508W for mDSCAM (mDSCAM-R508W) and examined cell adhesion formation similarly (Fig. 4*A* and *SI Appendix*, Fig. S7). The fluorescent imaging showed that the cell adhesion could be formed by this mutant (Fig. 4*B* and *SI Appendix*, Fig. S7*A*), consistent with results published before (36). However, no regular pattern was identified at the adhesion interfaces by EM (Fig. 4 *C* and *D* and *SI Appendix*, Fig. S7 *D* and *E*), and the intermembrane distance of the interface by the mutant was about 26 nm (Fig. 4*E*), larger than that for the wild type, implying that the conformation of the N-terminal Ig-like domains of mDSCAM, presumably the S-shaped conformation, might be disrupted by the mutation, similar to the reported data for dDSCAM1 (36). This result suggested that the conformation of the N-terminal Ig-like domains was also important for the *cis* assembly of mDSCAM.

The FnIII Domains Are Crucial for the Regular Pattern Formation and Membrane Interaction of mDSCAM. To further characterize the roles of different domains of mDSCAM in forming the regular pattern, we swapped the fragment of $D_{9–14}$ of mDSCAM (DM) with the counterpart of mDSCAML1 (DL) and generated two chimeric molecules referred as $DM_{1–8}$-$DL_{9–14}$-$DM_{15–16}$ (DM-DL-DM) and $DL_{1–8}$-$DM_{9–14}$-$DL_{15–16}$ (DL-DM-DL) (Fig. 5*A*). The adhesion interfaces formed by the two chimeric molecules were confirmed by fluorescent microscopy and then inspected by EM (Fig. 5 *B–D* and *SI Appendix*, Fig. S8). Interestingly, EM images showed that DL-DM-DL, rather than DM-DL-DM, could form a similar regular pattern to mDSCAM at the adhesion interfaces, suggesting that the fragment of $D_{9–14}$ of mDSCAM was crucial for inducing the regular pattern formation (Fig. 5 *C* and *D* and *SI Appendix*, Fig. S8 *D* and *E*). Furthermore, we also measured the intermembrane distances of the interfaces formed by the two chimeric molecules, showing that the width of the interface by DL-DM-DL was about 25 nm (Fig. 5*E*), relatively close to that of mDSCAM (Fig. 4*E*) and the width of the interface by DM-DL-DM was about 20 nm, similar to the width of mDSCAML1 (Figs. 3*M* and 5*E*), suggesting that the difference in the intermembrane distances between mDSCAM and mDSCAML1 might largely come from the region of $D_{9–14}$. This was consistent with the EM images showing that $D_{9–14}$ had different conformations for mDSCAM and mDSCAML1 (Fig. 1 *C* and *F* and *SI Appendix*, Fig. S1*D*).

The swapped fragments of $D_{9–14}$ of mDSCAM and mDSCAML1 contained four FnIII domains and two Ig-like domains. To further examine the roles of these domains within the fragment, we constructed several deletion mutants of the fragment of mDSCAM. But when the Ig-like domain D_9 or D_{14} was removed, the fragment could not be expressed properly, suggesting they might be important for the folding of the protein. Eventually two mutants were obtained, one was mDSCAM-$\Delta D_{10–11}$, where the first two FnIII domains were removed; the other was mDSCAM-ΔD_{12}, where the third FnIII domain was deleted (Fig. 5*A*). The adhesion formation by mDSCAM-$\Delta D_{10–11}$ and mDSCAM-ΔD_{12} was verified using fluorescent microscopy (Fig. 5*B* and *SI Appendix*, Fig. S8*A*), but no regular pattern was identified at the adhesion interfaces mediated by the two mutants under EM (Fig. 5 *C* and *D* and *SI Appendix*, Fig. S8 *D* and *E*), suggesting that the three FnIII domains might be important for the *cis* assembly of mDSCAM. The intermembrane distances for the two mutants were also measured. The width of mDSCAM-ΔD_{12}–mediated interfaces was about 34 nm (Fig. 5*E*), much larger than that of mDSCAM (Fig. 4*E*), and the width of mDSCAM-$\Delta D_{10–11}$–mediated interfaces was about 20 nm, smaller than that of mDSCAM (Figs. 4*E* and 5*E*). These results were not unexpected as the deletion of the FnIII domains would disrupt the hairpin-like conformation of the $D_{9–14}$ region (Fig. 1*C* and *SI Appendix*, Fig. S1*D*), thereby affect the *cis* assembly and the intermembrane distances.

As shown above, the last two FnIII domains, D_{15} and D_{16}, appeared to be dispensable for the regular pattern formation. However, the intermembrane distance of mDSCAM-$D_{1–14}$–mediated cell interface was about 28 nm (Fig. 4*E*), larger than the distance of the intact ectodomain of mDSCAM-$D_{1–16}$, implying that the last two FnIII domains could reduce the spacing between adjacent cells, probably by interacting with the cell membranes. Therefore, we expressed a fragment of mDSCAM containing $D_{15–16}$ in HEK293 cells and tested its interaction with lipids (43, 47). Indeed, the liposome pulldown assay showed that $D_{15–16}$ could be pulled down by the liposomes made of phosphocholine (Fig. 5*F*), a major component of the outer leaflet of the cell membrane. This was similar to the reported data for the sidekick molecules, which interacted with the cell membranes through the FnIII domains (43). The interaction of $D_{15–16}$ with the cell membrane might not only reduce the intermembrane spacing of mDSCAM, but also strengthen the interface by anchoring the molecules on the cell membranes.

Three-Dimensional Model of the Cell Adhesion Interface Mediated by mDSCAM. To visualize the 3D structure of the mDSCAM-mediated adhesion interface, ultrathin sections of the cellular samples prepared by HPF-FS were loaded onto the EM (Fig. 6*A*). The view showing the rod-like density pattern between the cell membranes was selected as the 0-degree view, where the rod-like densities had an angle of about 60 degrees relative to the cell membranes (Fig. 6*A*). Then a series of tomographic tilt images ranging from −65 degrees to 65 degrees were collected for 3D reconstruction (Movie S1). The resulting tomogram was segmented to generate 3D views of the adhesion interface (Fig. 6 *B* and *C* and Movie S1).

In the segmentation model, besides the regularly spaced tilt pattern that was well resolved at the 0-degree view (Fig. 6*C*), other regular patterns could also be visualized clearly at about −60 and +64 degrees, where the rod-like densities were connecting with each other, showing a continuous density along the middle zone between the adjacent cell membranes and the angles of the rod-like densities relative to the cell membranes were about 90 degrees (Fig. 6*C*), these views should correspond to the patterns identified in the EM images shown above (Fig. 2*G* and *SI Appendix*, Fig. S2). In other views, for example, at −30 or +30 degrees, no clear features could be seen at the interface (Fig. 6*C*). To verify the segmentation model, we collected several tomographic datasets from different adhesion interfaces, and the model could match the datasets reasonably well (*SI Appendix*, Fig. S10 and Movie S1).

Based on the segmentation result, a molecular model of the mDSCAM assembly at the adhesion interface was built by incorporating the information from the negative staining images as well as the mutagenesis and biochemical results (Fig. 7 and Movie S1). In the model, the N-terminal Ig-like domain region of the mDSCAM monomer, $D_{1–8}$, adopted an S-shaped conformation and the C-terminal tail region, $D_{9–16}$, had a hairpin-like conformation with $D_{15–16}$ interacting with the cell membranes (Fig. 7*A*). Two mDSCAM monomers from adjacent cells formed a homodimer with a double-S– shaped head (Fig. 7*A*), which was

similar to the crystal structure of the dDSCAM1-$D_{1–8}$ homodimer (36). The homodimeric model not only matched the intermembrane distance (~23 nm) measured from the tomograms of mDSCAM, it could also explain the variation of the intermembrane distances by the mDSCAM truncation mutants (Fig. 4*E*). For example, in the absence of $D_{15–16}$, the $D_{9–14}$ region might not be as proximal to the membrane surface, thus possibly resulting in a larger intermembrane distance. Indeed, the intermembrane distance of the mDSCAM-$D_{1–14}$–mediated interface was ~28 nm (Fig. 4*E*).

The resulting molecular model of the mDSCAM homodimers was fitted into the segmentation density (Fig. 7*B*) and generated a 2D assembly pattern of mDSCAM at the adhesion interface (Fig. 7*C*). The molecular model revealed the structure of mDSCAM assembly at different angles (Fig. 7*D* and Movie S1). Noticeably, at 0, −60, or 64 degrees, clear features that matched the corresponding tilt images and the segmentation densities could be visualized (Fig. 7*D*). Moreover, the model also provided clues for the interactions among the mDSCAM homodimers for forming the 2D assembly. At the 0-degree view, mDSCAM molecules connected with each other through the FnIII regions proximal to the cell membranes, and the last two FnIII domains, $D_{15–16}$, interacted with the cell membranes to strengthen the whole assembly (Fig. 7*D*). Unfortunately, due to the resolution limitation, the FnIII region with membrane proximity could not be resolved unambiguously in the tomograms.

At the −60 or 64-degree view, the *cis* interactions among the mDSCAM molecules appeared to occur through the double-S–shaped heads of mDSCAM homodimers (Fig. 7*D*), which corresponded to the continuous densities along the middle zone of the regular pattern at the interfaces in the EM images (Fig. 2*G* and *SI Appendix*, Figs. S2 and S10). This interaction might also be important for the *cis* pattern formation, as mDSCAM-R508W, a mutant that might abolish the S-shaped conformation of the N-terminal head, could not form the regular patterns at the interfaces (Fig. 4 *A–D*). However, mDSCAM-$D_{1–8}$ alone was insufficient to induce the regular pattern formation (Fig. 4 *A–D*), implying that the interactions between the double-S–shaped heads of mDSCAM homodimers might be relatively weak.

Taken together, the assembly model suggested that the N-terminal Ig-like domains were responsible for the *trans* interactions between cells, and they were also involved in the *cis* assembly of the pattern, and the tail or the FnIII region was important for the *cis* interaction of the molecules as well as the interaction with the cell membranes, which was consistent with both the mutagenesis data and the EM images shown above.

Discussion

Here we characterized the in situ structures of mDSCAM, mDSCAML1, and dDSCAMs at the cell adhesion interfaces and found that mDSCAM, rather than mDSCAML1 and dDSCAMs, formed a regular pattern at the adhesion interfaces. The formation of the regular pattern is mainly contributed by the ectodomain of mDSCAM, which can be roughly divided into three functional units: the N-terminal Ig-like domain region $D_{1–8}$, the middle region $D_{9–14}$, and the C-terminal region of the ectodomain $D_{15–16}$. The N-terminal region $D_{1–8}$ of mDSCAM adopts an S-shaped conformation as dDSCAM1, which might also be true for mDSCAML1. This is not surprising, as the domain

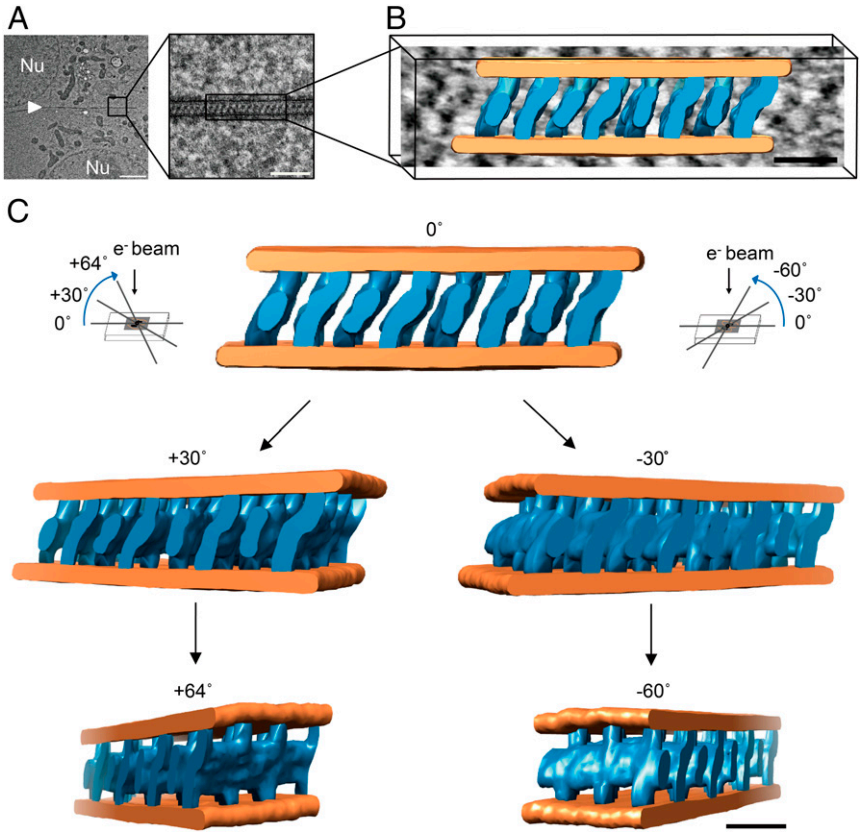

Fig. 6. Electron tomography and the segmentation model of the mDSCAM-mediated cell adhesion interface. (*A*) An EM image of the mDSCAM-mediated adhesion interface (*Left*, white arrowhead; Nu, nucleus). (Scale bar, 2 μm.) The enlarged image of the interface (black square) is shown on the *Right* (black rectangle). (Scale bar, 100 nm.) (*B*) The segmentation model of the adhesion interface mediated by mDSCAM with a tomogram slice superimposed on the background. (Scale bar, 25 nm.) The mDSCAM volume is colored in blue and the cell membranes are in orange. (*C*) Views of the segmentation model of the mDSCAM-mediated adhesion interface at different angles. (Scale bar, 20 nm.)

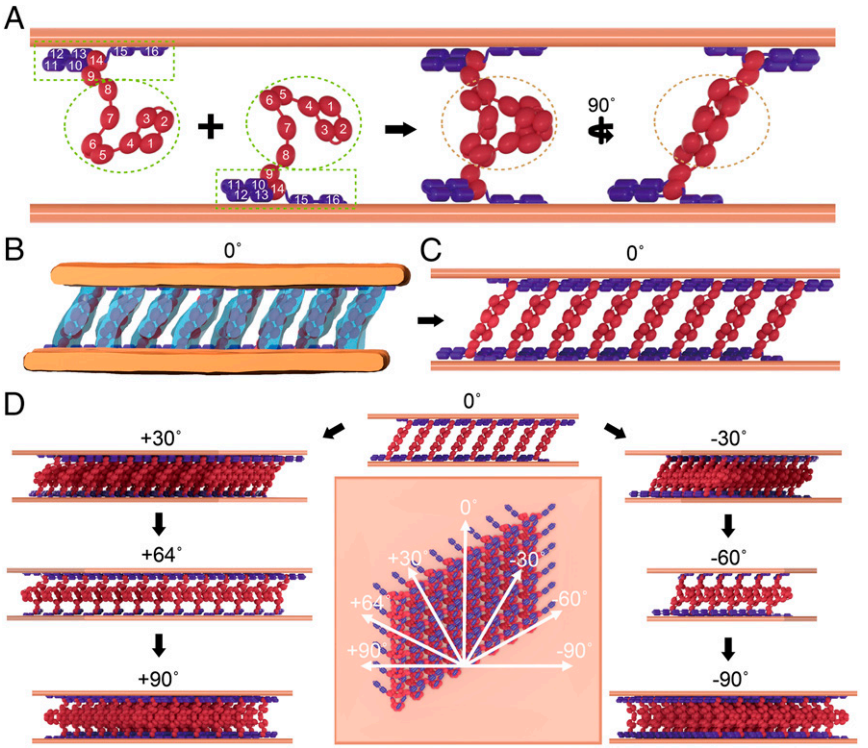

Fig. 7. Three-dimensional molecular model of the mDSCAM-mediated cell adhesion interface. (*A*) Two mDSCAM momoners (*Left*) from adjacent cell membranes form a homodimer (*Right*). The N-terminal Ig-like domain region ($D_{1–8}$) adopted an S-shaped conformation (dashed light green oval). The tail region ($D_{9–16}$) had a hairpin-like conformation (dashed light green rectangle) and $D_{15–16}$ is interacting with the cell membrane. The double-S–shaped heads of the homodimers are indicated by dashed orange ovals. (*B*) The model of the mDSCAM homodimer is fitted into the segmentation volume to generate a 3D model of the mDSCAM-mediated cell interfaces. (*C*) The 3D model of the mDSCAM-mediated cell interfaces. (*D*) Different views of the 3D model of the mDSCAM-mediated cell interfaces. The top view of the model (perpendicular to the cell membrane) and the view angles are shown in the *Center* (the segmentation volume of mDSCAM, blue; the cell membrane, orange; Ig-like domain, red; the FnIII domain, purple).

arrangements of DSCAM across species are quite similar (36, 48); thus, it would be reasonable to expect that the N-terminal double-S–shaped homodimers might be conserved among different species at the cell adhesion interfaces. According to the mutagenesis and EM data, the double-S–shaped heads of mDSCAM are involved in the *trans* adhesion interaction and the *cis* assembly of the regular pattern, although the interaction between the heads might be relatively weak.

Despite the similar conformations of the N-terminal heads, the intact ectodomains of DSCAMs displayed different conformations under EM, which are mainly due to the middle regions or the FnIII regions of the molecules. For mDSCAM, the $D_{9–16}$ region has a relatively stable hairpin-like conformation, while the $D_{9–16}$ fragment from mDSCAML1 appears to have a more open conformation, and the $D_{9–16}$ fragment of dDSCAM1 has the most flexible conformation among the three molecules. The EM data, especially the results from the mDSCAM/mDSCAML1 chimeric molecules, suggest that the $D_{9–14}$ region might be crucial for the regular pattern formation. The FnIII domains locating at the C-terminal end of the ectodomain of mDSCAM, $D_{15–16}$, are interacting with the cell membranes and might contribute to the stability of the interfaces, which is similar to previous results for the adhesion molecule sidekick (43) and EphA2 receptor (47).

It has been shown that the dysfunction of mDSCAM could lead to disorganization in neuron circuits in mice (26, 29, 30, 32, 49) and the defects largely depend on transhomophilic interaction of mDSCAM (50, 51). Although it is still unclear whether mDSCAM or mDSCAML1 functions similarly, a recent study shows that overexpression of the intracellular domain of mDSCAM, rather than mDSCAML1, decreases synapse numbers significantly (52). Given that the intracellular domain of mDSCAM is dispensable for the regular pattern formation, it is possible that the regular pattern formed by mDSCAM may regulate the organization of the intracellular domains as an outside-in signal. In addition, it has been shown that mDSCAM has a masking function by preventing the aggregation of other adhesion molecules at the interfaces (28) and is able to disassemble N-cadherin from cell–cell contacts (33). This could be correlated with the formation of the regularly assembled pattern of mDSCAM on the cell membranes. Notably, when mDSCAM and mDSCAML1 are coexpressed, the adhesion interfaces containing both molecules do not show the regular assembly pattern, but have a larger intermembrane distance, suggesting that they might interfere with each other in forming cell adhesion.

For *Drosophila*, dDSCAM1 has isoform-specific homophilic interactions and is involved in neuronal circuit assembly (53). Each neuron expresses several dDSCAM1 isoforms, resulting in unique identity of each neuron for self-avoidance (15, 54–56). Therefore, the dDSCAM1-mediated cell–cell adhesion might be more dynamic than the adhesion by mDSCAM, as the regular pattern formed at the interface would build a stable connection between cells, which might be unfavorable for self-avoidance of neurons. However, dDSCAM2 and dDSCAM4 have been shown to be able to direct dendritic targeting through adhesion (21) and dDSCAM2 can mediate axonal tiling through repulsion (22), but neither can form a regular pattern at the adhesion interfaces, suggesting that the correlation between the *cis* pattern formation and adhesion activities might be complex and needs to be elucidated in the future.

DSCAM has been implicated in Down syndrome for decades due to its overexpression in Down syndrome patients and the mouse models, and abnormal synaptic plasticity has also been

observed in patients and mice, although the mechanism is not fully understood (7, 57–59). It has been reported that the distribution of mDSCAM is developmentally regulated (60) and the DSCAM-mediated transsynaptic interaction might be important for the remodeling of mature synapses during long-term facilitation (LTF), an indicator of synaptic plasticity (23). Here we show that mDSCAM appears to be unique among the DSCAM homologs by forming an ordered assembly pattern, which might regulate cell adhesion in a different fashion. The overexpression of mDSCAM could modify the plasticity of neuron connections, thus affecting learning and memory. Overall, the assembly of mDSCAM at the adhesion interfaces may provide structural insights for understanding the role of DSCAM in regulating the neural network formation and in Down syndrome.

Materials and Methods

Cloning and Protein Expression and Purification. The full-length and the truncation mutants of mDSCAM (NM_031174.4) and mDSCAML1 (NM_001081270.1) were subcloned into the pTT5 vector fused with GFP or mCherry at the C terminus for fluorescent imaging. The mDSCAM truncation mutants were constructed by ligating the ectodomain fragments of mDSCAM ($D_{1–8}$, 1 to 782 amino acids [aa]; $D_{1–9}$, 1 to 883 aa; $D_{1–10}$, 1 to 985 aa; $D_{1–11}$, 1 to 1,087 aa; and $D_{1–14}$, 1 to 1,381 aa) with the transmembrane and cytoplasmic domain fragment (1,566 to 2,013 aa) by overlap PCR or homologous recombination using the ClonExpress MultiS One Step Cloning kit (Vazyme). The mDSCAM-ΔCyto construct was generated by deleting the sequence ranging from 1,624 aa to 2,013 aa. The constructs of mDSCAM-$\Delta D_{10–11}$ and mDSCAM-ΔD_{12} were made by deleting the sequence ranging from 884 to 1,084 aa and 1,088 to 1,185 aa, respectively. The mDSCAM/mDSCAML1 chimeric molecules, $DM_{1–8}$-$DL_{9–14}$-$DM_{15–16}$ and $DL_{1–8}$-$DM_{9–14}$-$DL_{15–16}$, were generated by swapping the mDSCAM sequence of 786 to 1,382 aa with the mDSCAML1 sequence of 845 to 1,444 aa. The point mutation R508W of mDSCAM was introduced by PCR. For protein expression, the fragments of mDSCAM-$D_{1–8}$ (1 to 784 aa), mDSCAM-$D_{9–16}$ (787 to 1,569 aa), mDSCAM-$D_{1–16}$ (1 to 1,569 aa), mDSCAM-$D_{15–16}$ (1,382 to 1,569 aa), mDSCAML1-$D_{1–8}$ (1 to 843 aa), mDSCAML1-$D_{9–16}$ (844 to 1,627 aa), and mDSCAML1-$D_{1–16}$ (1 to 1,627 aa) were subcloned into the pTT5 vector fused with a 6×His tag at the C terminus.

Drosophila DSCAM1 isoform 7.27.25.2 (a kind gift from L. Zipursky's laboratory) and the truncation mutants were subcloned into the pUAST vector (a kind gift from L. Zhang's laboratory) fused with GFP at the C terminus for fluorescent imaging. *Drosophila* DSCAM2 (NM_001274571.2), *Drosophila* DSCAM4 (NM_001274642.1), and *Aplysia* DSCAM (NM_001204542.1) were synthesized and also subcloned into the pUAST vector. The mutants of dDSCAM1 were produced by ligating the ectodomain fragments ($D_{1–8}$, 1 to 810 aa; $D_{1–9}$, 1 to 910 aa; $D_{1–10}$, 1 to 1,005 aa; $D_{1–13}$, 1 to 1,307 aa; and $D_{1–14}$, 1 to 1,402 aa) to the transmembrane and cytoplasmic domain fragment (1,591 to 2,031 aa). The mDSCAM/dDSCAM1 chimeric molecules were generated by swapping the ectodomain of mDSCAM (1 to 1,569 aa) with the ectodomain of dDSCAM1 (1 to 1,591 aa). For protein expression, the fragments of dDSCAM1-$D_{1–8}$ (1 to 810 aa), dDSCAM1-$D_{9–16}$ (810 to 1,591 aa), and dDSCAM1-$D_{1–16}$ (1 to 1,591 aa) were subcloned into the pFastBac1 vector (Invitrogen) fused with a 6×His tag at the C terminus, and the recombinant baculoviruses (Bac-to-Bac) were generated following the manufacturer's instruction.

Fragments of mDSCAM-$D_{1–8}$, mDSCAM-$D_{9–16}$, mDSCAM-$D_{1–16}$, mDSCAM-$D_{15–16}$, mDSCAML1-$D_{1–8}$, mDSCAML1-$D_{9–16}$, and mDSCAML1-$D_{1–16}$ were expressed in HEK293F cells cultured with Union 293 medium (Union-Biotech Co.) by transient transfection. Fragments of dDSCAM1-$D_{1–8}$, dDSCAM1-$D_{9–16}$, and dDSCAM1-$D_{1–16}$ were expressed in Hi5 cells cultured in ESF921 medium (Expression Systems) by recombinant virus infection. The supernatants were collected (8 d for HEK293F cells; 3 d for Hi5 cells) after the transfection and dialyzed against buffer (10 mM Tris, 150 mM NaCl at pH 8.0), then loaded onto Ni-NTA beads (Ni-NTA Superflow, Qiagen) and eluted with 250 mM imidazole (prepared with 10 mM Tris, 150 mM NaCl at pH 8.0). The eluted proteins were further purified by size exclusion chromatography with a HiLoad16/600 Superdex 200 pg gel filtration column (GE Healthcare) with running buffer (10 mM Tris, 150 mM NaCl at pH 8.0).

Negative Staining Electron Microscopy. Purified proteins (~10 μL) were applied to the glow-discharged EM carbon grids and stained with 0.75% (wt/vol) uranyl formate. The grids were loaded onto a 120-kV Tecnai T12 microscope (Thermo Fisher Scientific) for imaging. Images were acquired at a nominal magnification of 67,000× using a 4 k × 4 k Eagle charge-coupled device camera, corresponding to a pixel size of 1.74 Å/pixel on the specimen.

Liposome Pulldown Assay. For liposome preparation, 200 μL 1,2-dioleoyl-*sn*-glycero-3-phosphocholine (DOPC) (Avanti Lipids) (dissolved with chloroform, 25 mg/mL) was evaporated and hydrated in the buffer (150 mM NaCl, 50 mM Tris pH 7.4). Then the lipid suspension was loaded onto a Mini-Extruder (Avanti Lipids) and filtered through a 200-nm membrane to generate liposomes. About 400 ng proteins were added to 100 μL liposomes and incubated for 1 h at room temperature. The mixture was centrifuged at 16,000 × *g* for 30 min and the pellet was washed and resuspended in the hydration buffer twice. Then the pellet was loaded onto sodium dodecyl sulfate–polyacrylamide gel electrophoresis for Western blot and detected by mouse anti-His antibody (Proteintech) and goat anti-mouse IgG antibody conjugated with horseradish peroxidase (Proteintech) following the manufacturer's instructions.

Fluorescent Imaging and Confocal Microscopy. HEK293 cells or S2 cells grown on coverslips were transfected with the DSCAM constructs fused with GFP (mDSCAML1 fused with mCherry was used for cotransfection). After transfection (12 h of HEK293 cells; 48 h for S2 cells), the transfected cells were washed and fixed with 4% paraformaldehyde. The confocal images were acquired on a Leica SP8 microscope with a 63× oil immersion lens.

For CLEM, the cell culture dishes (Thermo Fisher Scientific) were marked with EM Finder grids (Gilder) by carbon evaporation (43) and coated with poly-L-lysine (Sigma). HEK293T cells were grown on the dishes overnight and transfected with the GFP-tagged DSCAM constructs. The fluorescent images were taken on an Olympus IX inverted microscope. The S2 cells were grown on glass-bottom dishes (Nest Biotechnology) with carbon markers prepared as described above and cotransfected with the GFP-tagged DSCAM constructs and a plasmid containing GAL4 gene. The transfected S2 cells were then imaged under a Zeiss LSM 710 microscope with a 63× oil immersion lens.

Chemical Fixation. The transfected cells grown on the marked dishes were washed and fixed with 2.5% glutaraldehyde in phosphate-buffered saline (PBS) for 1 h at 4 °C, then fixed with 1% osmium tetroxide (Ted Pella, Inc) in PBS for 1 h and subjected to dehydration with 30%, 50%, 70%, 85%, 95%, and 100% ethanol. Then the dehydrated cells were plastic embedded with 25%, 50%, 75%, and 100% Epoxy 812 (SPI-CHEM) at room temperature and solidified at 65 °C for 48 h.

High-Pressure Freezing and Freeze Substitution. A sapphire disc was marked by an EM Finder grid with carbon evaporation and coated with poly-L-lysine. HEK293T cells or S2 cells grown on the sapphire discs were transfected with the DSCAM constructs. Then the sapphire disc was transferred to an aluminum planchette and placed in the specimen holder for high-pressure freezing. HPF was carried out on a Wohlwend HPF Compact 2 high-pressure freezer (M. Wohlwend GmbH). The frozen specimens were transferred into cryotubes containing substitution solution (0.1% uranyl acetate, 0.6% water, and 1% osmium tetroxide and in acetone) at liquid nitrogen temperature followed by freeze substitution and plastic embedding (43).

Semithin and Ultrathin Sectioning. The resin blocks were trimmed according to the carbon marker, then semithin sections of 500-nm thickness were cut on a Leica EM UC7 ultra-microtome and stained with 0.5% (wt/vol) toluidine blue to visualize the target cells on an Olympus IX inverted microscope. Ultrathin sections of 100-nm thickness were also cut using a Leica EM UC7 ultra-microtome similarly and collected on carbon-coated copper grids. The ultrathin sections were stained with 3% uranyl acetate in 70% methanol aqueous solution and then by a modified Reynold's lead staining solutions (43, 44). The stained sections were imaged using a 120-kV Tecnai T12 microscope (Thermo Fisher Scientific).

Electron Tomography and Model Building. The ultrathin sections prepared by HPF-FS were loaded on a 120-kV Tecnai T12 microscope (Thermo Fisher Scientific) for 2D imaging and tilt series collection. Single axis tilt series were collected between −65° to +65° with 1° or 1.5° increment at a magnification of 67,000× using Xplore3D software (Thermo Fisher Scientific). Tomograms were calculated and segmented using the software IMOD (61, 62). The models of the Ig-like domains and the FnIII domains were generated according to the volumes of the domains from the known crystal structures and fitted into the segmentation volume manually. The 3D models of mDSCAM and the adhesion interface were built using the software Blender (https://www.blender.org) (63).

Data Availability. All study data are included in the article and/or supporting information.

ACKNOWLEDGMENTS. We thank the National Center for Protein Science Shanghai (Electron Microscopy and Integrated Laser Microscopy Systems) for their instrumental support and technical assistance. This work is supported by National Natural Science Foundation of China Grants 31470735, 31670747, and 91957102 (to Y.H.).

1. K. Yamakawa *et al*., DSCAM: A novel member of the immunoglobulin superfamily maps in a Down syndrome region and is involved in the development of the nervous system. *Hum. Mol. Genet.* **7**, 227–237 (1998).
2. R. A. Vacca *et al*., Down syndrome: Neurobiological alterations and therapeutic targets. *Neurosci. Biobehav. Rev.* **98**, 234–255 (2019).
3. Y. Saito *et al*., The developmental and aging changes of Down's syndrome cell adhesion molecule expression in normal and Down's syndrome brains. *Acta Neuropathol.* **100**, 654–664 (2000).
4. Z. Rahmani *et al*., Down syndrome critical region around D21S55 on proximal 21q22.3. *Am. J. Med. Genet. Suppl.* **7**, 98–103 (1990).
5. S. Bahn *et al*., Neuronal target genes of the neuron-restrictive silencer factor in neurospheres derived from fetuses with Down's syndrome: A gene expression study. *Lancet* **359**, 310–315 (2002).
6. K. Amano *et al*., Dosage-dependent over-expression of genes in the trisomic region of Ts1Cje mouse model for Down syndrome. *Hum. Mol. Genet.* **13**, 1333–1340 (2004).
7. M. Kazemi, M. Salehi, M. Kheirollahi, Down syndrome: Current status, challenges and future perspectives. *Int. J. Mol. Cell. Med.* **5**, 125–133 (2016).
8. D. Schmucker *et al*., Drosophila Dscam is an axon guidance receptor exhibiting extraordinary molecular diversity. *Cell* **101**, 671–684 (2000).
9. W. M. Wojtowicz, J. J. Flanagan, S. S. Millard, S. L. Zipursky, J. C. Clemens, Alternative splicing of Drosophila Dscam generates axon guidance receptors that exhibit isoform-specific homophilic binding. *Cell* **118**, 619–633 (2004).
10. W. M. Wojtowicz *et al*., A vast repertoire of Dscam binding specificities arises from modular interactions of variable Ig domains. *Cell* **130**, 1134–1145 (2007).
11. D. Hattori, S. S. Millard, W. M. Wojtowicz, S. L. Zipursky, Dscam-mediated cell recognition regulates neural circuit formation. *Annu. Rev. Cell Dev. Biol.* **24**, 597–620 (2008).
12. S. L. Zipursky, J. R. Sanes, Chemoaffinity revisited: Dscams, protocadherins, and neural circuit assembly. *Cell* **143**, 343–353 (2010).
13. M. E. Hughes *et al*., Homophilic Dscam interactions control complex dendrite morphogenesis. *Neuron* **54**, 417–427 (2007).
14. B. J. Matthews *et al*., Dendrite self-avoidance is controlled by Dscam. *Cell* **129**, 593–604 (2007).
15. B. E. Chen *et al*., The molecular diversity of Dscam is functionally required for neuronal wiring specificity in Drosophila. *Cell* **125**, 607–620 (2006).
16. T. Hummel *et al*., Axonal targeting of olfactory receptor neurons in Drosophila is controlled by Dscam. *Neuron* **37**, 221–231 (2003).
17. D. Hattori *et al*., Dscam diversity is essential for neuronal wiring and self-recognition. *Nature* **449**, 223–227 (2007).
18. H. He *et al*., Cell-intrinsic requirement of Dscam1 isoform diversity for axon collateral formation. *Science* **344**, 1182–1186 (2014).
19. S. S. Millard, Z. Lu, S. L. Zipursky, I. A. Meinertzhagen, Drosophila dscam proteins regulate postsynaptic specificity at multiple-contact synapses. *Neuron* **67**, 761–768 (2010).
20. V. Cvetkovska, A. D. Hibbert, F. Emran, B. E. Chen, Overexpression of Down syndrome cell adhesion molecule impairs precise synaptic targeting. *Nat. Neurosci.* **16**, 677–682 (2013).
21. W. Tadros *et al*., Dscam proteins direct dendritic targeting through adhesion. *Neuron* **89**, 480–493 (2016).
22. S. S. Millard, J. J. Flanagan, K. S. Pappu, W. Wu, S. L. Zipursky, Dscam2 mediates axonal tiling in the Drosophila visual system. *Nature* **447**, 720–724 (2007).
23. H.-L. Li *et al*., Dscam mediates remodeling of glutamate receptors in Aplysia during de novo and learning-related synapse formation. *Neuron* **61**, 527–540 (2009).
24. K. L. Agarwala *et al*., Cloning and functional characterization of DSCAML1, a novel DSCAM-like cell adhesion molecule that mediates homophilic intercellular adhesion. *Biochem. Biophys. Res. Commun.* **285**, 760–772 (2001).
25. P. G. Fuerst *et al*., DSCAM and DSCAML1 function in self-avoidance in multiple cell types in the developing mouse retina. *Neuron* **64**, 484–497 (2009).
26. P. G. Fuerst, A. Koizumi, R. H. Masland, R. W. Burgess, Neurite arborization and mosaic spacing in the mouse retina require DSCAM. *Nature* **451**, 470–474 (2008).
27. P. G. Fuerst *et al*, A novel null allele of mouse DSCAM survives to adulthood on an inbred C3H background with reduced phenotypic variability. *Genesis* **48**, 578–584 (2010).
28. A. M. Garrett, A. Khalil, D. O. Walton, R. W. Burgess, DSCAM promotes self-avoidance in the developing mouse retina by masking the functions of cadherin superfamily members. *Proc. Natl. Acad. Sci. U.S.A.* **115**, E10216–E10224 (2018).
29. F. M. Bruce, S. Brown, J. N. Smith, P. G. Fuerst, L. Erskine, DSCAM promotes axon fasciculation and growth in the developing optic pathway. *Proc. Natl. Acad. Sci. U.S.A.* **114**, 1702–1707 (2017).
30. A. B. Simmons *et al*., DSCAM-mediated control of dendritic and axonal arbor outgrowth enforces tiling and inhibits synaptic plasticity. *Proc. Natl. Acad. Sci. U.S.A.* **114**, E10224–E10233 (2017).
31. P. W. Keeley *et al*., Neuronal clustering and fasciculation phenotype in Dscam- and Bax-deficient mouse retinas. *J. Comp. Neurol.* **520**, 1349–1364 (2012).
32. S. Li *et al*., DSCAM promotes refinement in the mouse retina through cell death and restriction of exploring dendrites. *J. Neurosci.* **35**, 5640–5654 (2015).
33. N. Arimura *et al*, DSCAM regulates delamination of neurons in the developing midbrain. *Sci. Adv.* **6**, eaba1693 (2020).
34. M. Yamagata, J. R. Sanes, Dscam and Sidekick proteins direct lamina-specific synaptic connections in vertebrate retina. *Nature* **451**, 465–469 (2008).
35. D. Yimlamai, L. Konnikova, L. G. Moss, D. G. Jay, The zebrafish down syndrome cell adhesion molecule is involved in cell movement during embryogenesis. *Dev. Biol.* **279**, 44–57 (2005).
36. M. R. Sawaya *et al*., A double S shape provides the structural basis for the extraordinary binding specificity of Dscam isoforms. *Cell* **134**, 1007–1018 (2008).
37. R. Meijers *et al*., Structural basis of Dscam isoform specificity. *Nature* **449**, 487–491 (2007).
38. D. Studer, B. M. Humbel, M. Chiquet, Electron microscopy of high pressure frozen samples: Bridging the gap between cellular ultrastructure and atomic resolution. *Histochem. Cell Biol.* **130**, 877–889 (2008).
39. L. A. Baker, M. Grange, K. Grünewald, Electron cryo-tomography captures macromolecular complexes in native environments. *Curr. Opin. Struct. Biol.* **46**, 149–156 (2017).
40. K. L. McDonald, A review of high-pressure freezing preparation techniques for correlative light and electron microscopy of the same cells and tissues. *J. Microsc.* **235**, 273–281 (2009).
41. A. A. Mironov, G. V. Beznoussenko, Correlative microscopy: A potent tool for the study of rare or unique cellular and tissue events. *J. Microsc.* **235**, 308–321 (2009).
42. W. He, Y. He, Electron tomography for organelles, cells, and tissues. *Methods Mol. Biol.* **1117**, 445–483 (2014).
43. H. Tang *et al*., Architecture of cell-cell adhesion mediated by sidekicks. *Proc. Natl. Acad. Sci. U.S.A.* **115**, 9246–9251 (2018).
44. K. McDonald *et al*., "'Tips and Tricks" for high-pressure freezing of model systems" in *Methods in Cell Biology*, T. Müller-Reichert, Ed. (Academic Press, 2010), chap. 28, pp. 671–693.
45. W. He, P. Cowin, D. L. Stokes, Untangling desmosomal knots with electron tomography. *Science* **302**, 109–113 (2003).
46. H. Tanaka *et al*., Higher-order architecture of cell adhesion mediated by polymorphic synaptic adhesion molecules neurexin and neuroligin. *Cell Rep.* **2**, 101–110 (2012).
47. M. Chavent *et al*, Structures of the EphA2 receptor at the membrane: Role of lipid interactions. *Structure*, **24**, 337–347 (2016).
48. S. A. Armitage, R. Y. Freiburg, J. Kurtz, I. G. Bravo, The evolution of Dscam genes across the arthropods. *BMC Evol. Biol.* **12**, 53 (2012).
49. A. M. Garrett, A. L. Tadenev, Y. T. Hammond, P. G. Fuerst, R. W. Burgess, Replacing the PDZ-interacting C-termini of DSCAM and DSCAML1 with epitope tags causes different phenotypic severity in different cell populations. *eLife* **5**, e16144 (2016).
50. K. L. Agarwala, S. Nakamura, Y. Tsutsumi, K. Yamakawa, Down syndrome cell adhesion molecule DSCAM mediates homophilic intercellular adhesion. *Brain Res. Mol. Brain Res.* **79**, 118–126 (2000).
51. P. G. Fuerst, F. Bruce, R. P. Rounds, L. Erskine, R. W. Burgess, Cell autonomy of DSCAM function in retinal development. *Dev. Biol.* **361**, 326–337 (2012).
52. S. M. Sachse *et al*., Nuclear import of the DSCAM-cytoplasmic domain drives signaling capable of inhibiting synapse formation. *EMBO J.* **38**, e99669 (2019).
53. S. L. Zipursky, W. B. Grueber, The molecular basis of self-avoidance. *Annu. Rev. Neurosci.* **36**, 547–568 (2013).
54. G. Neves, J. Zucker, M. Daly, A. Chess, Stochastic yet biased expression of multiple Dscam splice variants by individual cells. *Nat. Genet.* **36**, 240–246 (2004).
55. P. Soba *et al*., Drosophila sensory neurons require Dscam for dendritic self-avoidance and proper dendritic field organization. *Neuron* **54**, 403–416 (2007).
56. S. K. Miura, A. Martins, K. X. Zhang, B. R. Graveley, S. L. Zipursky, Probabilistic splicing of Dscam1 establishes identity at the level of single neurons. *Cell* **155**, 1166–1177 (2013).
57. M. Rachidi, C. Lopes, "Mental retardation and human chromosome 21 gene overdosage: From functional genomics and molecular mechanisms towards prevention and treatment of the neuropathogenesis of Down syndrome" in *Genomics, Proteomics, and the Nervous System*, J. D. Clelland, Ed. (Springer, New York, 2011), pp. 21–86.
58. R. J. Siarey, A. J. Villar, C. J. Epstein, Z. Galdzicki, Abnormal synaptic plasticity in the Ts1Cje segmental trisomy 16 mouse model of Down syndrome. *Neuropharmacology* **49**, 122–128 (2005).
59. R. J. Siarey *et al*., Increased synaptic depression in the Ts65Dn mouse, a model for mental retardation in Down syndrome. *Neuropharmacology* **38**, 1917–1920 (1999).
60. G. B. de Andrade, L. Kunzelman, M. M. Merrill, P. G. Fuerst, Developmentally dynamic colocalization patterns of DSCAM with adhesion and synaptic proteins in the mouse retina. *Mol. Vis.* **20**, 1422–1433 (2014).
61. D. N. Mastronarde, Dual-axis tomography: An approach with alignment methods that preserve resolution. *J. Struct. Biol.* **120**, 343–352 (1997).
62. J. R. Kremer, D. N. Mastronarde, J. R. McIntosh, Computer visualization of three-dimensional image data using IMOD. *J. Struct. Biol.* **116**, 71–76 (1996).
63. G. T. Johnson, S. Hertig, A guide to the visual analysis and communication of biomolecular structural data. *Nat. Rev. Mol. Cell Biol.* **15**, 690–698 (2014).